Research Square

Preprints are preliminary reports that have not undergone peer review.
They should not be considered conclusive, used to inform clinical practice,
or referenced by the media as validated information.

Micro-topological and Micro-mechanical investigation of compressibility in polydisperse granular assemblies: a 2D DEM study

Rezig Ahlem

ahlem.rezig@univ-setif.dz

University of Ferhat

Mansouri Mouloud

Ferhat Abbas University of Setif Setif

José Gregorio Gutiérrez Chacón

Universidad Politécnica de Madrid (UPM)

Research Article

Keywords: Granular materials, Discrete Element Method (DEM), compressibility, Inter-particle friction, Polydispersity

Posted Date: November 24th, 2026

DOI: https://doi.org/10.21203/rs.3.rs-10731530/v1

License: This work is licensed under a Creative Commons Attribution 4.0 International License.
Read Full License

Additional Declarations: No competing interests reported.

Micro-topological and Micro-mechanical investigation of compressibility in polydisperse granular assemblies: a 2D DEM study

Author Information

Rezig Ahlem*
Department of Civil Engineering, Emerging Materials Research Unit
University of Ferhat Abbas Setif 1
Setif, 19000, Algeria
ORCID: https://orcid.org/0009-0000-4836-4514

Mansouri Mouloud
Civil Engineering Research Laboratory of Setif (LRGCS)
Department of Civil Engineering
Ferhat Abbas University of Setif
Setif, 19000, Algeria
ORCID: https://orcid.org/0000-0002-4179-7488

José Gregorio Gutiérrez Chacón
Departamento de Ingeniería y Morfología del Terreno
Escuela Técnica Superior de Ingenieros de Caminos, Canales y Puertos
Universidad Politécnica de Madrid (UPM)
Madrid, 28040, Spain
Email: jg.gutierrez@upm.es
ORCID: https://orcid.org/0000-0002-9498-5888

Corresponding Author

Rezig Ahlem
Department of Civil Engineering
Emerging Materials Research Unit
University of Ferhat Abbas Setif 1
Setif, 19000, Algeria
Email: **ahlem.rezig@univ-setif.dz**

Acknowledgments
No funding was received for conducting this study.

Abstract

The mechanical behaviour of granular materials depends on several parameters, including the properties of intergranular interactions at the particle scale and the fabric at the mesoscopic scale. This study investigates the micro-topological origins of macroscopic compressibility in granular assemblies, focusing on the combined impact of inter-particle friction and size polydispersity. 2D DEM simulations of isotropic compression were performed across a range of friction coefficients and distinct particle size distributions. The simulations show that increasing the confining stress decreases the global void ratio, increases the mechanical coordination number, and reduces the fraction of rattler particles, while the compressibility response is characterized by distinct recompression and virgin compression stages. Initially looser packings, whether induced by higher interparticle friction or a narrower particle size distribution, exhibit greater virgin compressibility. Contact-network analysis reveals that the global void ratio is governed by the topology of elementary loops, with interparticle friction promoting larger loop structures that preserve local voids. A wider particle size distribution enhances global packing through a pore-filling mechanism but also generates pronounced local packing heterogeneity, characterized by the coexistence of densely packed regions and local void pockets. Finally, force-chain analysis shows that the strongest contact forces are predominantly transmitted through well-confined particles in dense regions, although bridge particles spanning local void pockets may also participate in force transmission.

Keywords: Granular materials; Discrete Element Method (DEM); compressibility; Inter-particle friction; Polydispersity.

Introduction

Granular materials are commonly encountered in both natural environments and industrial processes. They are also the main components of geotechnical structures such as dams, foundation supports, and embankments. Despite their widespread presence, predicting their mechanical behavior remains challenging due to the complex relationship between macroscopic response and the underlying discrete particle interactions. For non-cohesive soils, the rheological behavior is strongly governed by the arrangement and geometry of the grains, as highlighted by Salot et al.(2009).

Macroscopic compressibility, defined as the capacity of a granular assembly to rearrange into denser configurations under applied stress, is controlled by its internal fabric and meso-scale topological structures (Fu et al., 2021; Shen et al., 2017). These structures are characterized by the organization of particle contacts and the spatial distribution of

voids. In this context, the Discrete Element Method (DEM) has emerged as a powerful tool, enabling direct tracking of particle trajectories and inter-particle forces that are not accessible through conventional experimental techniques (Cundall & Strack, 1979).

At the particle scale, inter-particle friction (μ) plays a fundamental role in determining the stability and configuration of granular assemblies. Compression requires particles to slide and rotate, processes that must overcome frictional resistance (T. Zhang et al., 2020). Numerical investigations have shown that increasing the intergranular friction coefficient leads to the formation of looser packings with higher void ratios, as friction acts as a locking mechanism that inhibits particle rearrangement (Nguyen & Vo, 2023). Conversely, lower friction coefficients promote particle mobility, which facilitates rearrangement and leads to denser assemblies (Che et al., 2025; T. Zhang et al., 2020) . Although higher friction enhances peak shear strength ratios, its influence on the critical state shear strength ratio is generally limited, as the material reaches a fully frictional regime at large strains (Salot et al., 2009). In parallel, the polydispersity of sizes, defined as the variation in grain sizes within a granular assembly, has a significant influence on the packing structure and density. In polydisperse systems, smaller particles can fill the spaces between larger grains, reducing free space and increasing the packing density (Liu et al., 2023) and (Che et al., 2025) . The degree of particle size dispersion, often expressed as the ratio of the maximum particle radius to the minimum particle radius, is inversely proportional to the minimum void ratio that can be achieved (Nguyen & Vo, 2023). Consequently, polydisperse assemblies tend to exhibit higher coordination numbers and greater connectivity than monodisperse systems, which improves structural stability.

Despite these advances, the combined influence of inter-particle friction and size polydispersity on the mesoscale organisation of granular materials and their macroscopic compressibility remains understudied and still requires detailed analysis. In particular, the mechanisms by which these parameters jointly influence the coordination number, void distribution, force chains, and loop structures have not yet been fully clarified. It is therefore essential to address this gap in order to improve predictive modeling of the behaviour of granular materials under various loading conditions.

The mechanical behaviour of granular assemblies can be characterized using several microstructural indicators. A brief description of common indicators is provided below. One such indicator is the coordination number, which is defined as the average number of contacts per particle and is a key parameter for assessing structural stability and failure behaviour (Nawaz & Combe, 2021). Force chains emerge from this contact network as preferential pathways that carry the majority of the applied load, forming the material's structural backbone (Zhu et al., 2016a). Network-based approaches model particles as nodes and contacts as edges. This enables graph-theoretical metrics, such as clustering coefficients and degree centrality, to be used to quantify the internal organisation of the

system (Papadopoulos et al., 2018). While early investigations focused primarily on two-dimensional photoelastic systems, recent DEM studies have extended these analyses to more complex configurations. For instance Liu et al.(2023) demonstrated that topological descriptors, such as the shortest path length and network diameter, can offer valuable insights into how granular structures evolve under different loading conditions. At the mesoscale, loops defined as closed arrangements of particles in contact play a crucial role in stabilising force chains and providing lateral confinement. In two-dimensional systems, these loops can be interpreted as polygonal void cells that link load-bearing grains (Bagi, 1996; Kuhn, 1999), or as structural elements that prevent force chain buckling and enhance overall stability (Liu et al., 2023; Zhu et al., 2016a).

This study investigates the coupled effects of inter-particle friction and size polydispersity on the compressibility of granular assemblies using 2D DEM simulations under isotropic compression. A comprehensive multiscale framework integrating global and local descriptors is adopted, including the mechanical coordination number, rattler fraction, force-chain characteristics, loop topology, and local void ratio derived from Voronoi tessellation.

While these descriptors have each been examined individually in prior work, this study shows that interparticle friction and narrow particle size distribution despite acting through distinct physical mechanisms converge on the same topological signature, characterized by a shift toward larger elementary loops, which explains their similar effect on virgin compressibility. Building on this, the study establishes a quantitative statistical link between local topological disorder, characterized through Voronoi tessellation, and contact-force partitioning, analyzed using hexbin stress–topology mapping, across varying levels of polydispersity (C_u) and inter-particle friction (μ). By demonstrating that a broader particle size distribution simultaneously enhances global packing efficiency while inducing greater local geometric disorder and modifying the spatial organization of force transmission, this study provides new micromechanical insights into the structural origins of granular compressibility, contributing to the development of more reliable predictive models for granular materials in geotechnical applications.

2. Discrete Element Method (DEM)

2.1.DEM methodology

The Discrete Element Method (DEM), originally developed by Cundall and Strack (1979), models granular materials as assemblies of discrete particles interacting at contact points. To simplify the geometry of the elements, disks are often used in 2D simulations and spheres in 3D (Jiang et al., 2015).The method alternates between applying the contact law and integrating the equations of motion. The most commonly used algorithm for integrating particle motion equations is the Velocity-Verlet incremental scheme (Allen & Tildesley, 2017; Mansouri, 2014)**.** The translational motion of a particle i of mass m_i and position x_i is governed by the second Newton's law expressed as:

$$m_i \ddot{x}_i = \sum_{j \neq i} \mathrm{F}_{ij}^{\text{contact}} + m_i \mathrm{g} \tag{1}$$

Where:m_i is the mass of particle i,$\ddot{x}_i$ is the translational acceleration of particle i,$F_{ij}^{contact}$ is the contact force exerted by particle j on particle i,g is the gravitational acceleration.

$$I_i \ddot{\phi}_i = \sum_{j \neq i} M_{ij}^{\text{contact}} \tag{2}$$

Where I_i is the moment of inertia, $\ddot{\phi}_i$ the angular acceleration and M_{ij}^{contact} is the torque generated by the contact force exerted by particle j on particle i

When particles come into contact, they undergo slight deformation; in this study, the interaction is modeled using a smooth interaction approach, where the contact forces are related to this deformation. Contacts are detected by calculating the normal distance between two grains, D_n (Fig. 1). A contact is considered to exist if $D_n \leq 0$. In this case, D_n is referred to as "overlap."

The total contact force is decomposed into normal and tangential components. In this work, the normal component is by the linear viscoelastic law (Mansouri, 2014):

$$\mathrm{F}_n = (-k_n D_n - \nu_n V_n)\hat{n} \tag{3}$$

where k_n is the normal stiffness, ν_n is the normal damping coefficient, V_n is the relative normal velocity, and $\hat{n}$ is the unit normal vector pointing from particle i to j.

The tangential contact force follows Coulomb's friction law. To correctly distinguish between static friction (stick) and kinetic friction (slip), a trial force is calculated first (Khellaf & Mansouri, 2024):

$$\mathrm{F}_{s,\text{trial}} = -k_s D_s - \nu_s V_s \tag{4}$$

where k_s and ν_s are the tangential stiffness and damping coefficient respectively, D_s and V_s are the relative tangential displacement and velocity respectively.

The actual tangential force F_s is then limited by the Coulomb criterion:

$$\mathrm{F}_s = \begin{cases} \mathrm{F}_{s,\text{trial}} & \text{if } |\mathrm{F}_{s,\text{trial}}| \leq \mu |\mathrm{F}_n| \\ \mu |\mathrm{F}_n| \cdot \mathrm{sgn}(\mathrm{F}_{s,\text{trial}}) & \text{if } |\mathrm{F}_{s,\text{trial}}| > \mu |\mathrm{F}_n| \end{cases} \tag{5}$$

In which μ is the coefficient of friction.

Energy dissipation during collisions is primarily related to the damping coefficient ν_n. From a practical standpoint, it is preferable to express this damping in terms of the coefficient of restitution ε_n, which corresponds to the ratio of the particle's velocity before and after a collision, such that $0 \leq \varepsilon_n \leq 1$. These two coefficients are related by the following equation:

$$\nu_n = \frac{-2\ln(\varepsilon_n)}{\pi}\sqrt{k_n m_{\text{eff}}} \tag{6}$$

where the effective mass of two contacting particles is:

$$m_{\text{eff}} = \frac{m_i m_j}{m_i + m_j} \tag{7}$$

The numerical stability of the simulation requires the time step Δt to be smaller than a fraction of the contact duration. In the viscoelastic model, the contact duration is approximated as (Mansouri, 2014):

$$t_c = \pi\sqrt{\frac{m_{\text{eff}}}{k_n}} \tag{8}$$

leading to the critical time step:

$$\Delta t_{\max} \approx 0.1 t_c = 0.1\pi\sqrt{\frac{m_{\text{eff}}}{k_n}} \tag{9}$$

which is applied throughout this study.

Finally, because idealized disks and spheres tend to underestimate shear strength by allowing unrealistically free rolling, a rolling resistance moment is incorporated into the mode(Arroyo et al., 2011; Zhang & Wang, 2015). Following the approach described by Saidani et al. (2022), the rolling resistance torque opposing relative rotation is defined as:

$$M_{r,ij} = -\mu_r |\mathrm{F}_n| R_{\text{eff}} \frac{\omega'}{|\omega'|} \tag{10}$$

where $\omega' = \omega_i - \omega_j$ is the relative angular velocity, μ_r is the rolling friction coefficient, and R_{eff} is the effective rolling radius.

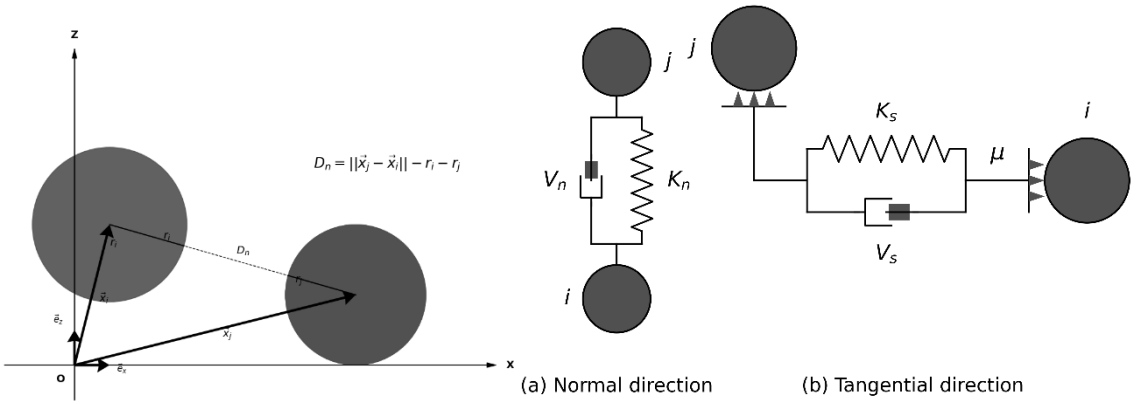

Figure 1. Contact forces models: **a** normal force model, **b** tangential force model

It is important to note that the model is implemented using the C programming language, which handles the core computations and simulations of the system. OpenGL toolkit is employed solely for the visualization of the model, enabling interactive and real-time observation of the particles and their behaviour. For the presentation and analysis of the results, Python is used to process the simulation output and generate plots.

2.2. Sample preparation

Particles were placed one by one at random positions without initial overlaps until the target particle count and initial distribution were attained. Specifically, the narrow distribution ($C_u = 1.33$) comprised 2913 grains, the medium distribution ($C_u = 1.80$) comprised 3847 grains, and the wide distribution ($C_u = 3.09$) comprised 4337grains. The specific diameter distributions are depicted in the particle size distributions in Figure 2.

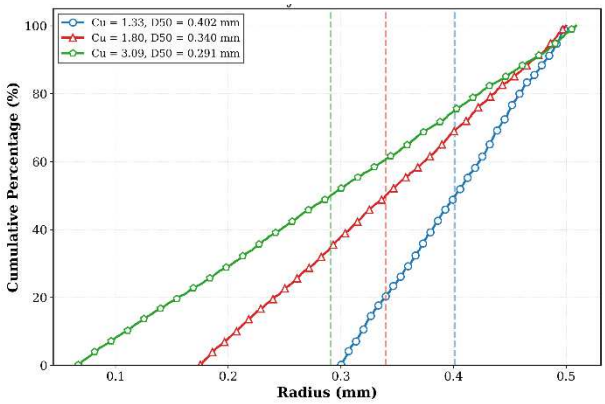

Figure 2. Particle size distributions (narrow $C_u = 1.33$, medium $C_u = 1.80$, and wide $C_u = 3.09$)

Initial packings were generated using a sequential placement algorithm within a periodic 2D box of side length 0.05 m. To account for the inherent stochastic variability of the random particle generation process, five independent samples were generated for each simulation condition using different random seeds. *The macroscopic compression curves presented in Section 4.1 correspond to the average of five independent realizations. All subsequent microstructural analyses presented in Sections 4.2–4.5 are illustrated for a single representative realization*.

2.3. Compression tests

Once generated, the test specimens are subjected to isotropic compression under controlled stress, as depicted in Figure 3. The desired stress is achieved by adjusting the displacement in a servo-controlled manner. For each compression level, the compressive stress is gradually increased to the target stress, then held constant until quasi-static equilibrium is reached. Static equilibrium is considered to have been reached when the difference between the void ratios corresponding to two consecutive time steps is less than 10^{-8}. The applied compressive stress levels ranged from 10 kPa to 10 MPa. In the tests conducted, the applied compressive stress levels ranged from 10 kPa to 10 MPa for each coefficient of friction ranging from 0 to 0.8. Gravitational

acceleration is set to zero, and the coefficient of friction between the grains and the walls is likewise set to zero.

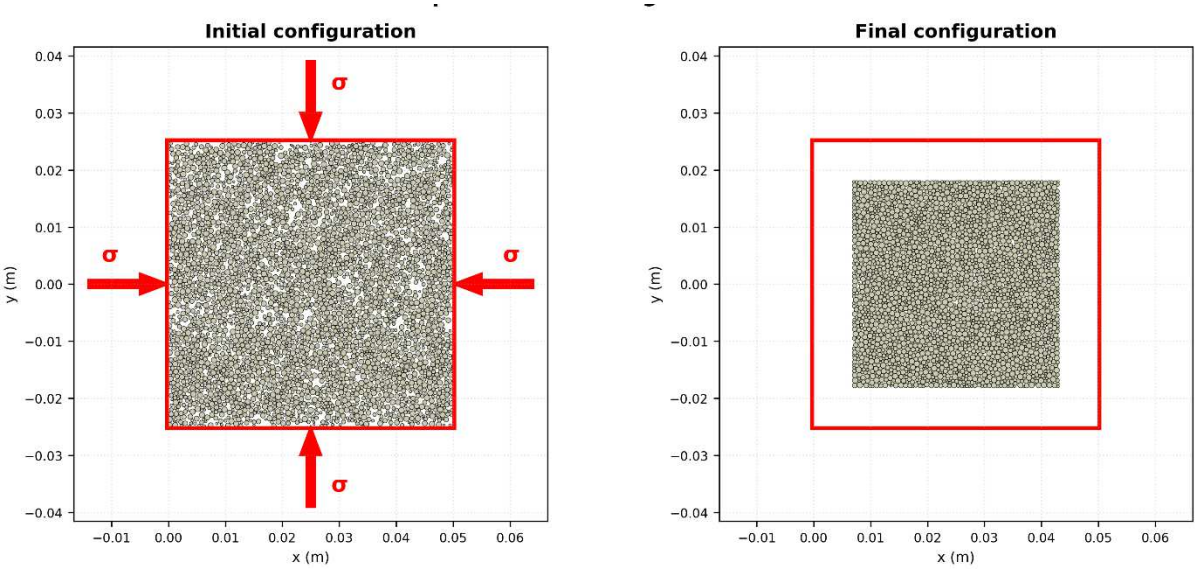

Figure 3. DEM sample: initial loading scheme and final state

The micromechanical properties (Table 1) of the soil particles used in the DEM simulations were selected to ensure that the resulting contact overlap remained minimal relative to the particle size, consistent with the rigid-body approximation underlying the linear contact law (Eq. 3). In the numerical model, the stiffness parameters were implemented as $k_g = k_m = 4.0 \times 10^8$ N/m for the normal components and $k_s = 3.2 \times 10^8$ N/m for the tangential component (i.e., $k_s = 0.8 \times k_g$). These values were chosen to be sufficiently high so that the overlap was kept negligibly small across the tested stress range (up to 10 MPa). Furthermore, the corresponding critical timestep (Eq. 9) remained numerically tractable.

Table 1: Input parameters for DEM simulations

Parameter	Symbol	Value
Particle density	ρ_s	2650 kg/m^3
Normal stiffness	k_n	4×10^8 N/m
Shear stiffness	k_s	3.2×10^8 N/m
Friction coefficient	μ	Variable (0.0 – 0.8)
Contact normal stiffness of walls	k_n	4×10^8 N/m
Intergranular Friction(particle-walls)	μ	0.0

3. Micro-Structural Characterization Framework

To interpret the underlying physics of the macroscopic compressibility, a multi-scale characterization framework is employed. The granular assembly is analyzed in relation to three distinct aspects: particle connectivity (i.e., mechanical coordination number

(Z_{mech}) and rattlers), the network topology (tessellation and loop analysis), and the local volume distribution (Voronoi analysis).

3.1 Mechanical Coordination Number and Rattler Fraction

The stability of granular materials is governed by their connectivity. While the mean coordination number (Z) represents the average number of contacts per particle, it often overestimates the structural stability due to the presence of rattler particles with zero or minimal contacts that do not participate in force transmission.

To strictly quantify the active contact network, the Mechanical Coordination Number (Z_{mech}) is adopted, defined following the criterion of Thornton (2000):

$$Z_{mech} = \frac{2N_c - N_1}{N_p - N_1 - N_0} \tag{11}$$

where N_c is the total number of contacts, N_p is the total number of particles, and N_1 and N_0 represent the number of particles with one and zero contacts, respectively. The Rattler Fraction (ϕ_r) is defined as the proportion of these non-active particles relative to the total population ($(N_0 + N_1)/N_p$). The evolution of ϕ_r provides a direct metric of the jamming state of the material as noted by O'Hern et al. (2003). The transformation of rattler particles into load-bearing particles and their incorporation into the force-chain network represents a key mechanism governing densification under external loading.

3.2 Topological Analysis: Network Tessellation and Loop Distributions

Beyond simple connectivity, the geometric arrangement of particles is analyzed using network tessellation. The contact network is viewed as a graph in which the centers of the particles are nodes and the contact branches are edges. By decomposing this graph into constituent polygons, the loop size distribution $P(L)$ is obtained. A loop of size $L = 3$ corresponds to a stable triangular configuration, which is the elementary unit of a rigid, isostatic packing. Loops with $\text{with } L > 3$ (quadrilaterals, pentagons, etc.) represent local topological defects or holes in the fabric. As proposed by Radjai et al. (1998) and recently by Zhu et al. (2016a) , the presence of larger loops ($L \geq 6$) is a signature of the system's transition toward instability and dilatancy. Following the framework of Tordesillas (2007), these loops provide the necessary lateral confinement to prevent force chain buckling. This topological tessellation is used to explain the macroscopic bulking effect: a shift in $P(L)$ toward larger values indicates a transition from a dense, triangular lattice to a loose, arch-supported structure that characterizes volumetric expansion.

3.3 Force Chain Heterogeneity

The transmission of stress through the granular medium is analyzed via PDF of the normal contact forces (F_n). Following the framework of Radjai et al. (1998), all forces are normalized by the mean normal force, $f = F_n/\langle F_n \rangle$, to provide a dimensionless basis for comparison. The contact network is partitioned into a bimodal structure: The Weak Network ($f < 1$): Contacts carrying forces below the global average. The Strong Network

($f > 1$): Contacts carrying forces greater than the mean. The statistical heterogeneity of the strong network is characterized by the tail of the distribution, which is expected to follow an exponential decay:

$$P(f) = k \cdot e^{\beta(1-f)} \tag{12}$$

Where k represents the normalization constant, corresponding to the probability density at the transition point where the force equals the mean (i.e., at $f = 1$). β is the decay exponent (or heterogeneity parameter). It characterizes the width of the force distribution; a lower value of β indicates a longer tail, implying a more heterogeneous system with a higher probability of finding extremely large forces. The degree of stress concentration is further quantified by the coefficient of variation ($COV = \sigma/\langle F_n \rangle$), where σ is the standard deviation.

3.4 Local and Global Void Ratio via Voronoi Tessellation

To link the global void ratio e to local structural variations, particularly for polydisperse assemblies,Voronoi tessellation is employed. Each particle i is assigned a Voronoi cell V_i i.e. the region of space closer to the centroid of that particle than to any other particle. The local void ratio for particle i is defined as:

$$e_{local,i} = \frac{V_{v,i}}{V_{p,i}} = \frac{V_i - V_{p,i}}{V_{p,i}} \tag{13}$$

Where $V_{p,i}$ is the volume of the particle itself (the area in 2D model) and $V_{v,i}$ is the volume of voids in the Voronoi cell surrounding the particle.

This method, used by Voivret et al.(2007) and Alshibli & El-Saidany (2001), enables the spatial distribution of porosity to be characterized.While global measurements average these values, the Voronoi analysis reveals the statistical spread (heterogeneity) of packing density. The mean and standard deviation of e_{local} across all interior particles (excluding cells touching the boundaries) provide quantitative measures of geometric disorder.

Based on equation (13), the global void ratio for a given volume of the assembly can be expressed in terms of the local void ratios associated with the grains as:

$$e = \frac{\sum_{Np} V_{v,i}}{\sum_{Np} V_{p,i}} = \frac{\sum_{Np} e_{local,i} V_{p,i}}{\sum_{Np} V_{p,i}} \tag{14}$$

Where Np is the number of particles in the assembly. In the case of a monodisperse assembly, the individual particle volume $V_{p,i}$ becomes constant; consequently, the global void ratio given by this equation equals the arithmetic average of the local void ratios, i.e. $e = \sum_{Np} e_{local,i}/Np$.

In the case of a polydisperse assembly, local void ratios in equation (14) are weighted by the individual particle volumes; therefore, when small particles are associated with the highest local void ratios, the global void ratio becomes lower than the arithmetic average

of the local void ratios. The opposite is expected if the highest local void ratios are associated with large particles.

4. Analysis and Results

4.1 Macroscopic Compressibility and Coordination Evolution

Figure 4 illustrates the evolution of macroscopic response parameters of granular samples subjected to isotropic compression for different interparticle friction coefficients (μ). The plotted curves correspond to the average over five independent realizations, with shaded bands indicating ± one standard deviation. As shown in Figure 3(a), the void ratio (e) is plotted against the logarithm of the confining stress ($\log \mathrm{P}$). The semi-logarithmic relationship captures the characteristic recompression and virgin compression stages, where the void ratio decreases progressively with increasing stress. A clear dependency on friction is observed: the frictionless assembly ($\mu = 0.00$) achieves the densest packing state, while increasing friction significantly inhibits particle rearrangement, resulting in looser packings with higher void ratios across all stress levels. In contrast, increasing friction significantly prevents initial densification, resulting in looser packing structures. This behavior is widely supported by previous research, which shows that higher interparticle friction acts as a stabilizing factor that promotes the persistence of open, porous microstructures that are highly resistant to compression (Nguyen & Vo, 2023; Zhang et al., 2021; Zhang et al., 2020). The plots in Figure 4a can also be used to calculate the compression index ($\mathrm{C_c}$), which characterizes the slope of the compression curve for the virgin state on the semi-logarithmic graph. The calculation results indicate that $\mathrm{C_c}$ increases steadily as friction increases, ranging from 0.118 to 0.137. The frictionless assembly ($\mu = 0.00$) has the lowest compressibility ($C_c = 0.118$), while the high-friction assembly ($\mu = 0.80$) has the highest compressibility index ($C_c = 0.137$). This positive correlation between interparticle friction and the macroscopic compression index is well supported by Zhang et al. (2021). This could be explained by the fact that assemblies with higher friction initially form looser, metastable structures. Once the stress is sufficient to overcome tangential contact resistance, the porous network experiences substantial volumetric collapse through particle sliding and rearrangement. Conversely, the frictionless assemblies are already in a dense, geometrically locked state prior to yielding, leaving much less available void space for further contraction.

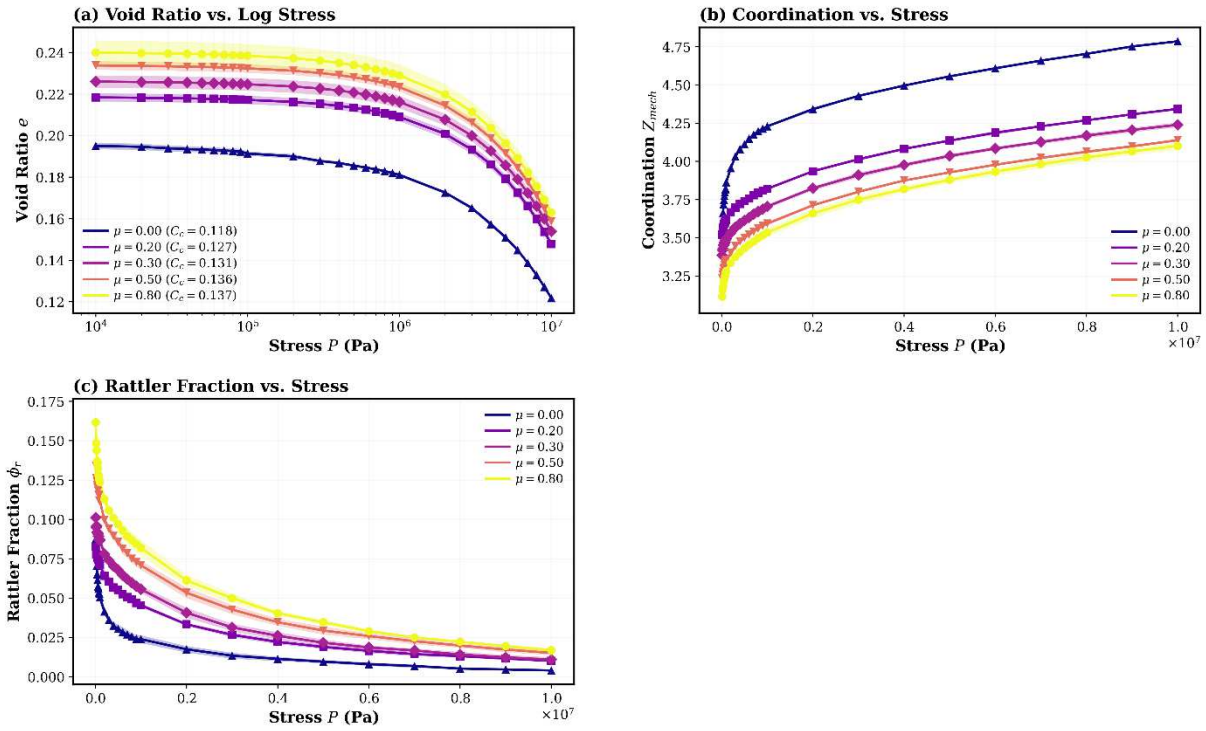

Figure 4. Influence of inter-particle friction coefficient (μ) on multi-scale isotropic compression behaviour: (a) Void ratio (e) vs. confining stress (p) in semi- logarithmic axis system; (b) Mechanical coordination number Z_{mech} vs. confining stress (p), (c) Rattler fraction Φ_r vs. confining stress (p).

Figure 4(b) shows the evolution of the mechanical coordination number (Z_{mech}) with the compression stress. For the frictionless case ($\mu = 0.00$), Z_{mech} increases steadily with stress, reaching a highly connected state of approximately 5.0 at maximum confinement. This approaches the theoretical isostatic limit for perfectly frictionless spheres, where purely geometric interlocking and high connectivity are required to ensure mechanical stability (Agnolin & Roux, 2007; Monti et al., 2022). Conversely, as μ increases, the coordination number required to maintain stability drops significantly, reaching only $Z_{mech} \approx 4.01$ for the highly frictional case ($\mu = 0.80$) at the same stress level. This shift illustrates a clear transition from geometric stability to frictional stability, where strong tangential contact forces allow the granular skeleton to support the applied macroscopic stresses despite having a significantly lower particle connectivity.

Figure 4(c) illustrates the evolution of the rattler particles fraction (ϕ_r) as the compressive stress increases. The sharp exponential decay of rattlers at low stress levels signifies the rapid engagement of floating particles into the force network. Notably, high-friction assemblies maintain a slightly higher fraction of rattlers at equivalent stress levels, suggesting that frictional arching shields pockets of particles from the global stress field.

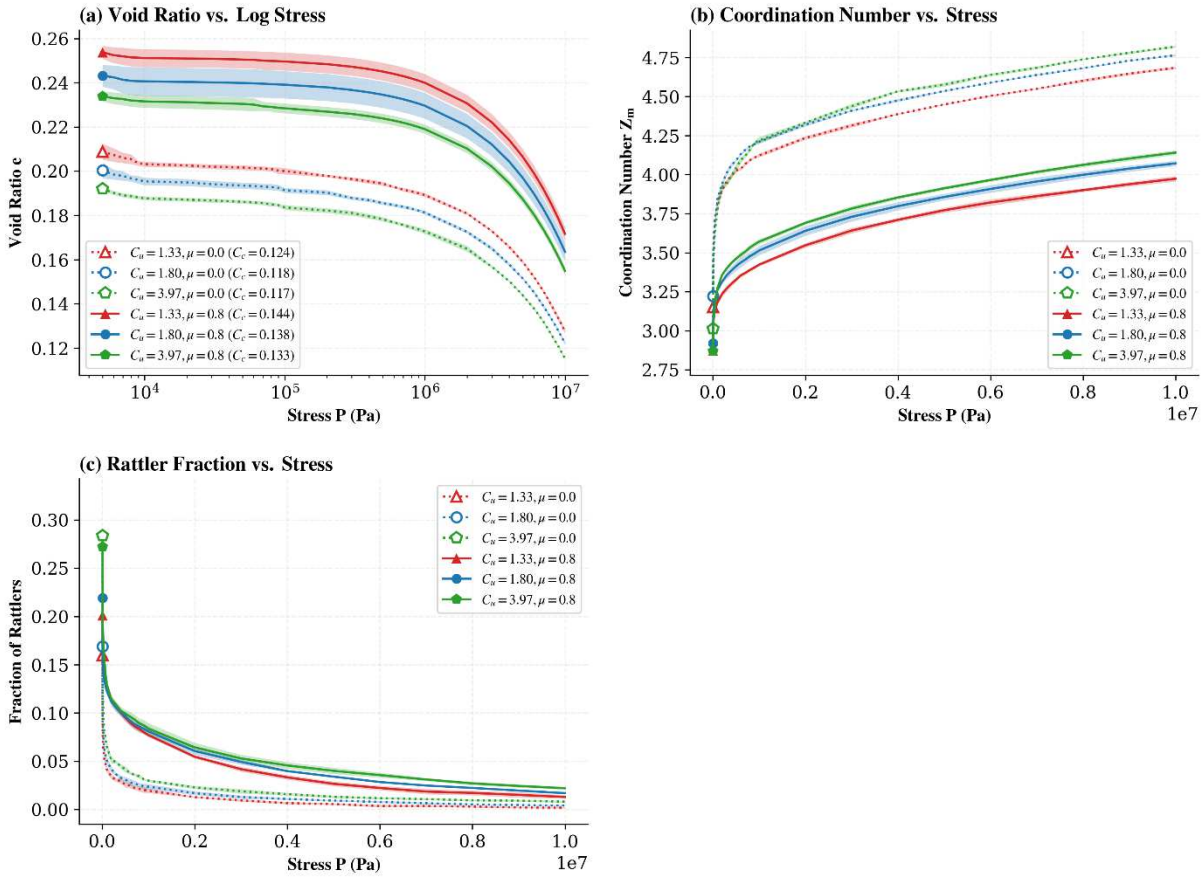

Figure 5. Multi-scale response as a function of increasing confinement stress for narrow, medium, and the wide PSDs, and interparticle friction coefficients of 0.00 and 0.80. (a) Void ratio (e) vs. confining stress (p) in semi- logarithmic axis system; (b) Mechanical coordination number Z_{mech} vs. confining stress (p), (c) Rattler fraction Φ_r vs. confining stress (p).

The influence of size polydispersity was evaluated by comparing three distinct particle size distributions (PSDs), quantitatively expressed by their coefficient of uniformity (C_u = 1.33, 1.80, and 3.09). As illustrated in Figure 5, the assemblies with wider size distributions (C_u = 1.80 and 3.09) consistently achieve a denser packing state characterized by a lower void ratio (e) across all stress levels compared to the more uniform assembly (C_u = 1.33). This observation aligns with established DEM literature, which states that higher C_u values (i.e., broader size distributions) enhance packing density through the pore-filling action of finer grains (Azéma et al., 2017; He et al., 2022). The influence of size polydispersity was evaluated by comparing three distinct particle size distributions (PSDs), quantitatively expressed by their coefficient of uniformity ($C_u = 1.33, 1.80$, and 3.09). As illustrated in Figure 5, the assemblies with wider size distributions ($C_u = 1.80$ and 3.09) consistently achieve a denser packing state characterized by a lower void ratio (e) across all stress levels compared to the more uniform assembly ($C_u = 1.33$). This observation aligns with established DEM literature, which states that higher C_u values (i.e., broader size distributions) enhance packing density through the pore-filling action of finer grains (Azéma et al., 2017; He et al., 2022). From a mechanical standpoint, this difference in compaction is attributed to a mechanism of “partial pore filling”: in

assemblies with higher C_u, the smaller particles, which are more abundant, occupy the interstitial voids created by the larger particles. In contrast, the more uniform assembly ($C_u = 1.33$) lacks these finer fractions, resulting in a more porous packing structure with larger unoccupied intergranular voids

Figure 5(a) especially shows that the assembly with narrow size distribution ($C_u = 1.33$) consistently exhibits higher compression indices (C_c), regardless of the coefficient of friction (μ). For $\mu = 0.0$, $C_c = 0.124$ for the $C_u = 1.33$ assembly, 0.118 for $C_u = 1.80$, and 0.117 for $C_u = 3.09$. For $\mu = 0.8$, $C_c = 0.144$ for $C_u = 1.33$, 0.138 for $C_u = 1.80$, and 0.133 for $C_u = 3.09$. Again, this indicates that the initially looser structure undergoes greater volumetric compression during plastic deformation, whether this looser structure is achieved by increasing the coefficient of friction or is due to a narrow particle size distribution.

Regarding geometric connectivity, Figure 4(b) shows the evolution of the mechanical coordination number (Z_m), where broader distributions maintain higher connectivity compared to $C_u = 1.33$, with $C_u = 1.80$ exhibiting the highest level overall.

However, for the rattler fraction (f_{rattler}) (Figure 4(c)), we observe that, in the absence of friction ($\mu = 0.0$), f_{rattler} tends toward the same value regardless of whether the particle size distribution is narrow or wide; conversely, for a friction coefficient $\mu = 0.8$, f_{rattler} remains higher for broader particle size distributions (peaking for $C_u = 3.97$). In fact, for these broader distributions, the number of small particles that remain shielded from the overall force-transmission chains is higher.

4.2 Topological Origins of Void Ratio

In order to study the effect of compression on microscopic geometry, the loop topology of the contact network is analyzed. Figure 7 illustrates the graphical distribution of the contact network loops for frictionless ($\mu = 0.0$) and high-friction ($\mu = 0.8$) assemblies, for narrow, intermediate, and wide particle size distributions ($C_u = 1.33$,1.80, and 3.09), at a compressive stress level of 1 MPa. Whereas, the corresponding PDFs for loop sizes ($P(L)$) are shown in Figure 6. These figures show clearly that structural topology is closely related to interparticle friction. For the frictionless assembly ($\mu = 0.0$), the topology is dominated by triangular loops ($L = 3$), which constitute the majority of the contact network. As shown in Figure 7, for $\mu = 0.0$, $L = 3$ loops account for 48.6% of the contact network for $C_u = 1.33$, 49.1% for $C_u = 1.80$, and 50.7% for $C_u = 3.09$. This predominance of $L = 3$ loops corresponds to the dense packing indicated by the low rate of macroscopic voids in Figures 4 and 5. This observation is consistent with simulations that concluded that the number of triangles increases sharply at the moment of locking during isotropic compression of frictionless assemblies(Arévalo, Zuriguel, & Maza, 2010; Arévalo, Zuriguel, Trevijano, et al., 2010). In fact, in the complete absence of friction, the particles experience zero resistance to tangential sliding and effortlessly rearrange toward the

most compact local configuration, i.e., triangular structures, as reported by Kruyt and Rothenburg(2014).

In contrast, introducing a high friction coefficient ($\mu = 0.8$) fundamentally alters the topology. The distribution widens considerably, with a marked decrease in the number of triangular loops (from about 50% to $33.3\% - 36.0\%$ across the grain size distributions) and an increase in the number of larger loops ($L > 4$). This indicates that friction allows for the formation of large polygonal loops ($L \geq 4$) capable of supporting external loads. In the absence of friction, these polygons tend to collapse, forming more compact triangular loops characteristic of denser structures(Meng et al., 2018; Silbert et al., 2002).Non-triangular loops that form stable arcs around open spaces result, from a macroscopic standpoint, in higher void ratios.

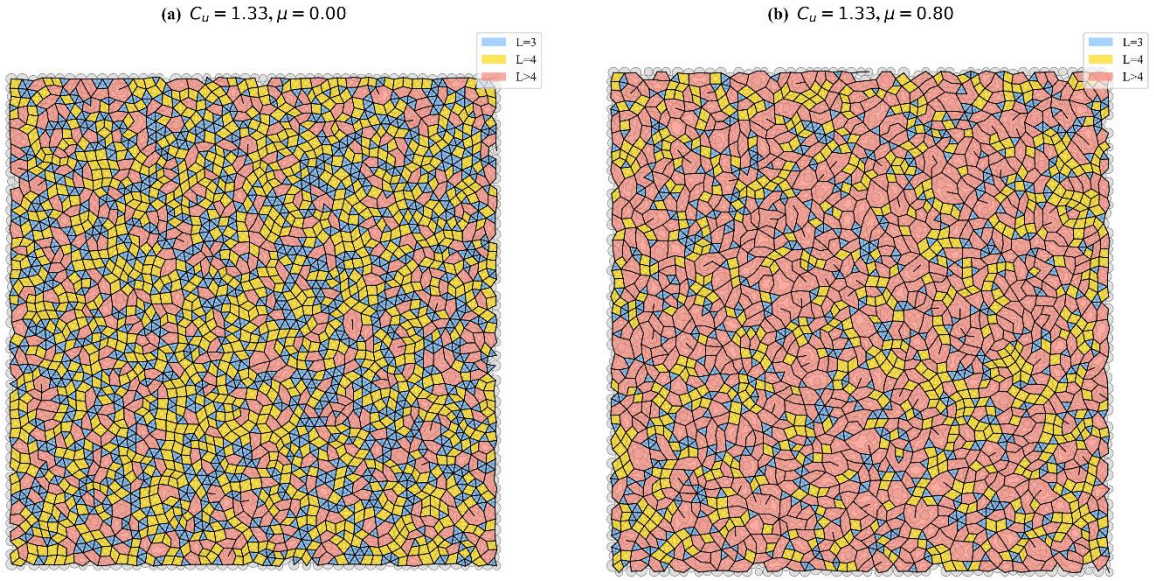

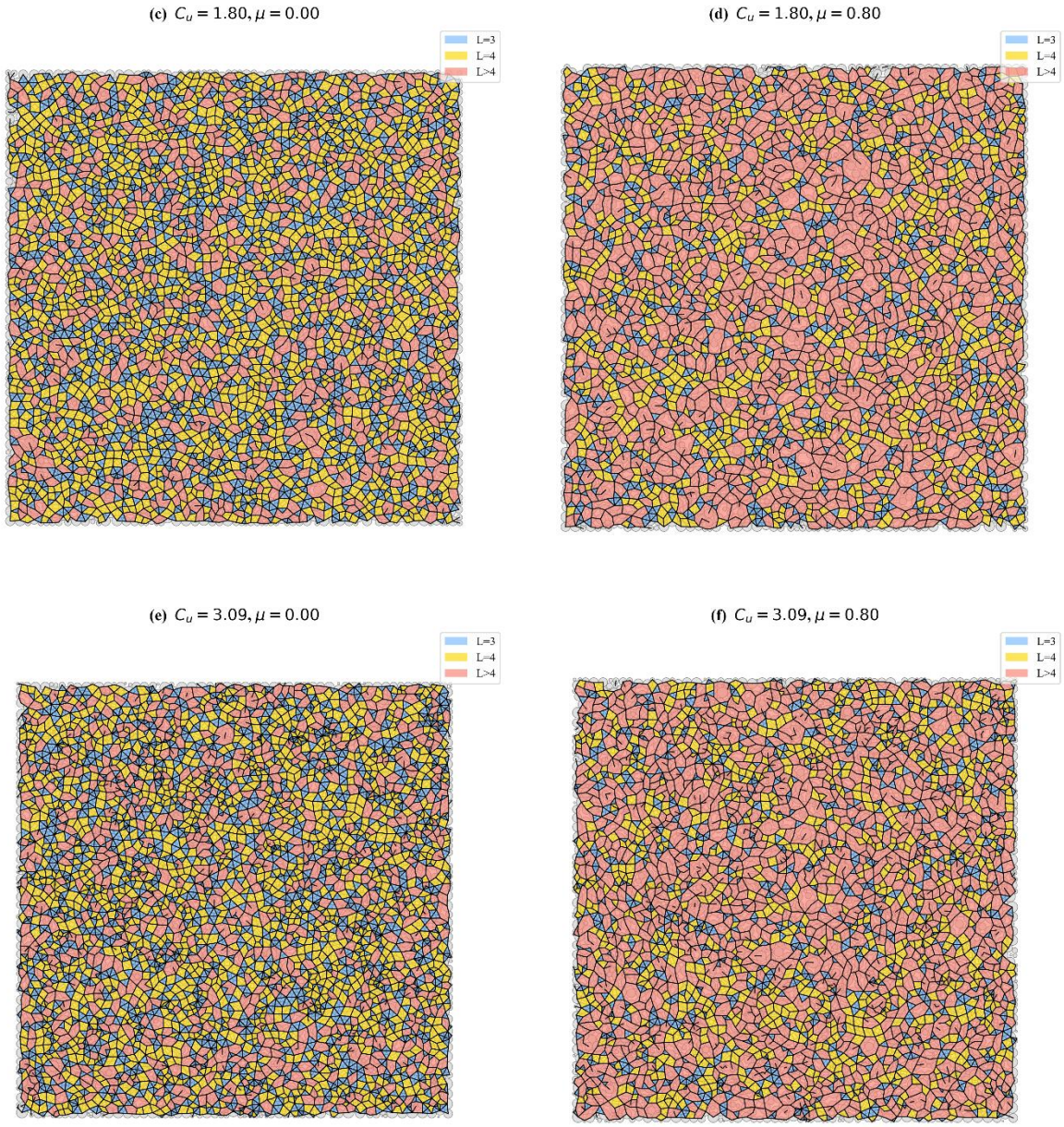

Figure 6. Graphical distribution of the contact network loops at a compressive stress level of 1*MPa*, for wide and narrow PSDs, without and with friction **(a)** ($C_u = 1.33, \mu = 0.00$), **(b)** ($C_u = 1.33, \mu = 0.80$), **(c)** ($C_u = 1.80, \mu = 0.00$), **(d)** ($C_u = 1.80, \mu = 0.80$), **(e)** ($C_u = 3.09, \mu = 0.00$), **(f)** ($C_u = 3.09, \mu = 0.80$).

When comparing the particle size distributions ($C_u = 1.33$,1.80, and 3.09), in the absence of friction ($\mu = 0.0$), the distribution of loops remains quite similar, with the widest distribution ($C_u = 3.09$) showing a slightly higher proportion of triangular loops (50.7%) compared to $C_u = 1.80$ (49.1%) and $C_u = 1.33$ (48.6%). However, in the presence of friction ($\mu = 0.8$), triangular loops are slightly less frequent in the narrow distribution (33.3% for $C_u = 1.33$, compared to 35.8% for $C_u = 1.80$ and 36.0% for $C_u = 3.09$); consequently, larger loops ($L > 4$) are more frequent in narrower distributions. This is consistent with the observations made earlier regarding this distribution, namely a higher

void ratio, a lower coordination number, and a higher compression index due to the collapse of larger voids during plastic deformation (normal compression).

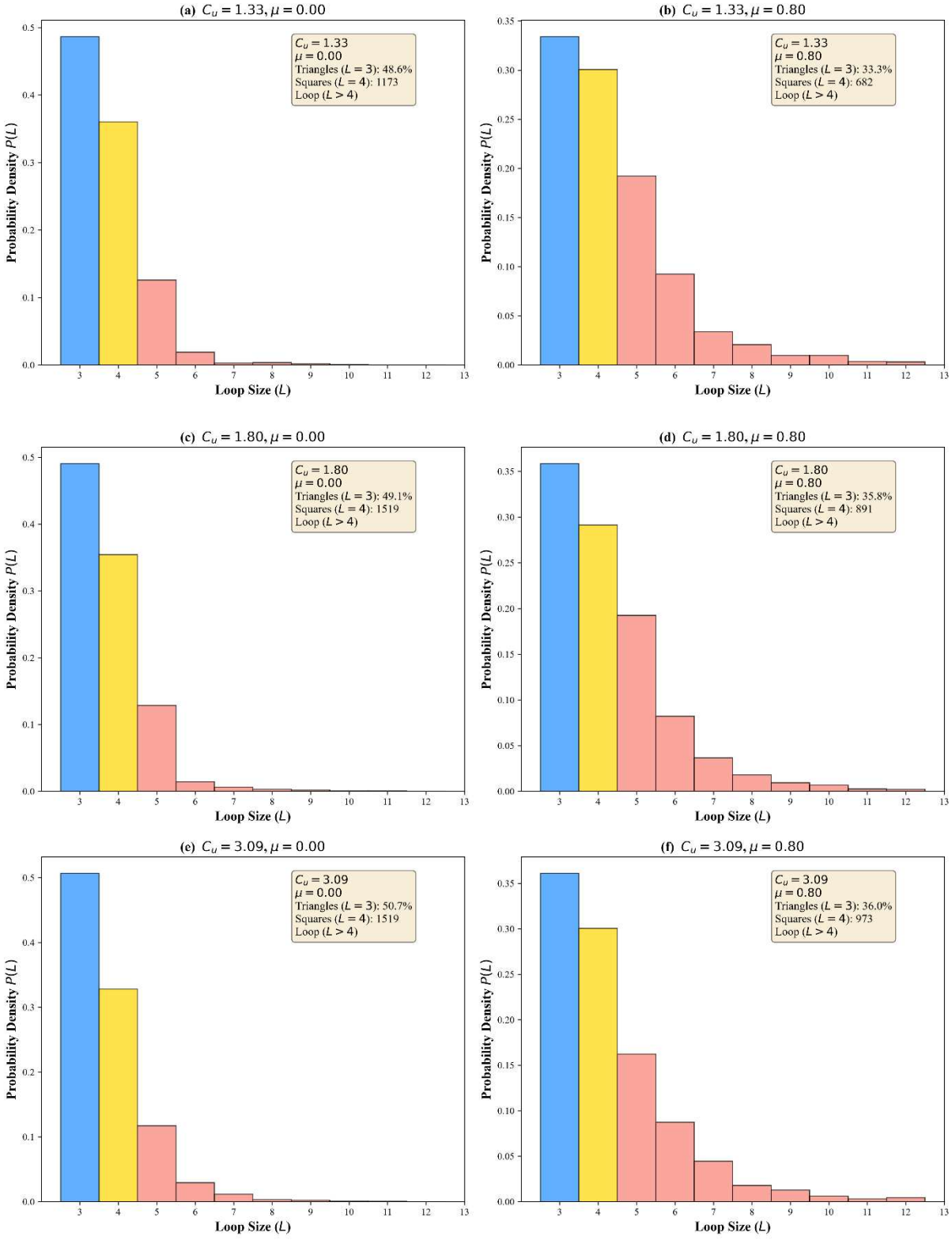

Figure 7. Probability density $P(L)$ of loop sizes at a compressive stress level of 1 MPa, for wide, intermediate, and narrow PSDs, without and with friction: **(a)** ($C_u = 1.33, \mu = 0.00$),

(b) $(C_u = 1.33, \mu = 0.80)$, **(c)** $(C_u = 1.80, \mu = 0.00)$, **(d)** $(C_u = 1.80, \mu = 0.80)$, **(e)** $(C_u = 3.09, \mu = 0.00)$, **(f)** $(C_u = 3.09, \mu = 0.80)$.

4.3 Force Chain Heterogeneity and Stress Transmission

The macroscopic response and topological transitions observed in the previous sections are fundamentally rooted in the statistical heterogeneity of the internal force network. To quantify this, Figures 7 and 8 present the probability density functions (PDF) of the normalized normal contact forces $F_n/\langle F_n \rangle$ at equilibrium under a compressive stress of 1*MPa*. Following the framework established by Radjai et al. (1998), the contact network is partitioned into three functional regimes based on force magnitude: the sub-mean (passive) network ($F_n/\langle F_n \rangle < 1$), the active bridge network ($1.0 < F_n/\langle F_n \rangle < 1.5$), and the super-mean backbone ($F_n/\langle F_n \rangle > 1.5$).

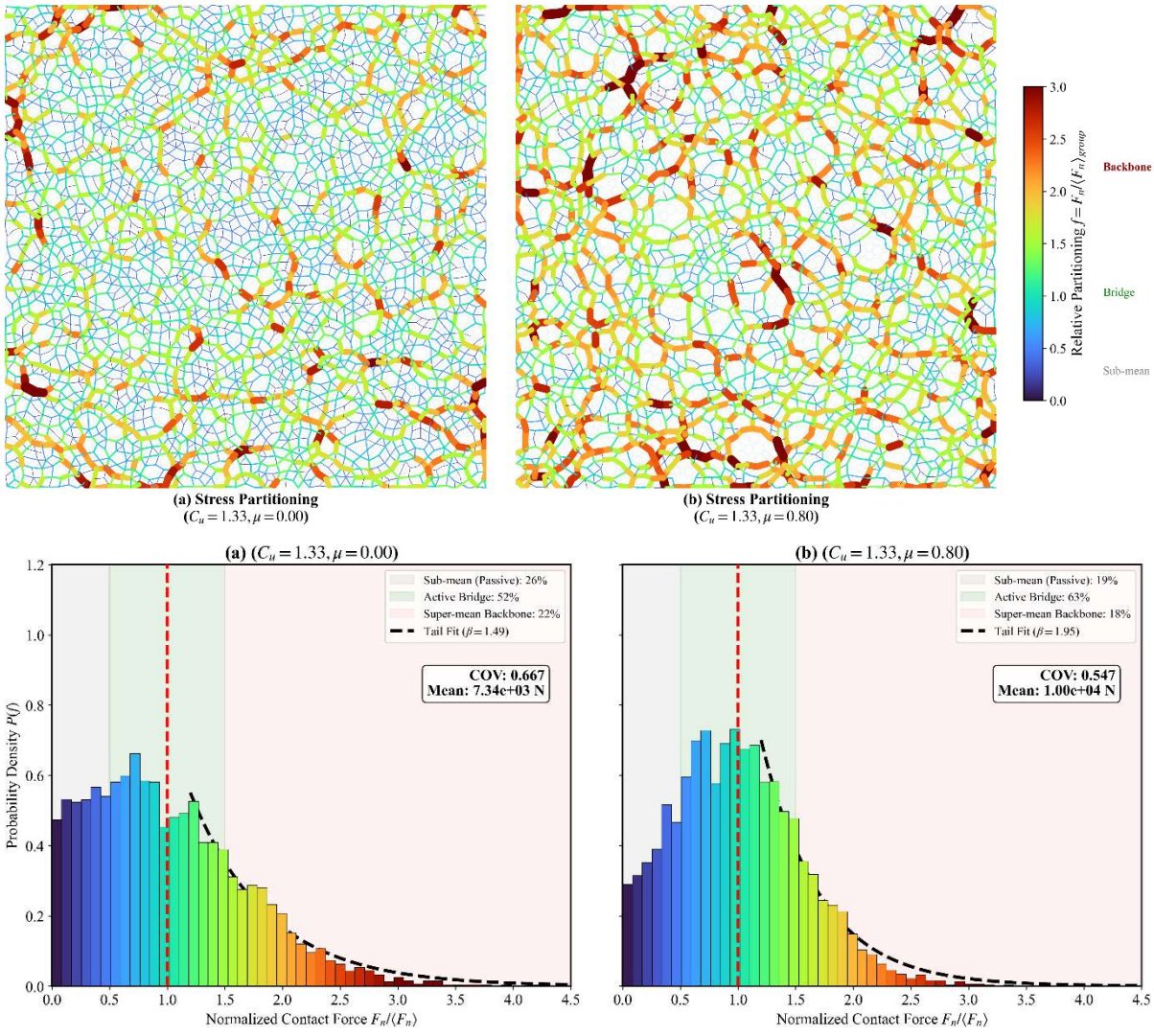

Figure 8. Force chain networks and force probability distributions for narrow PSD ($C_u = 1.33$) assembly with interparticle friction coefficients of 0.00 and 0.80.

Analysis of the force chains and their probability densities presented in Figures 7,8 and 9 leads to the following observations. Across all particle size distributions ($C_u = 1.33$,1.80, and 3.09), when friction is introduced, the number of contacts decreases; consequently, the number of branches

in the force network decreases and the average contact force increases. Furthermore, the sub-mean (passive) network and the over-mean network decrease, while the active bridge network increases. This change causes the distribution of forces to become more concentrated around the mean, leading to a decrease in covariance coefficient and an increase of the tail fit coefficient.

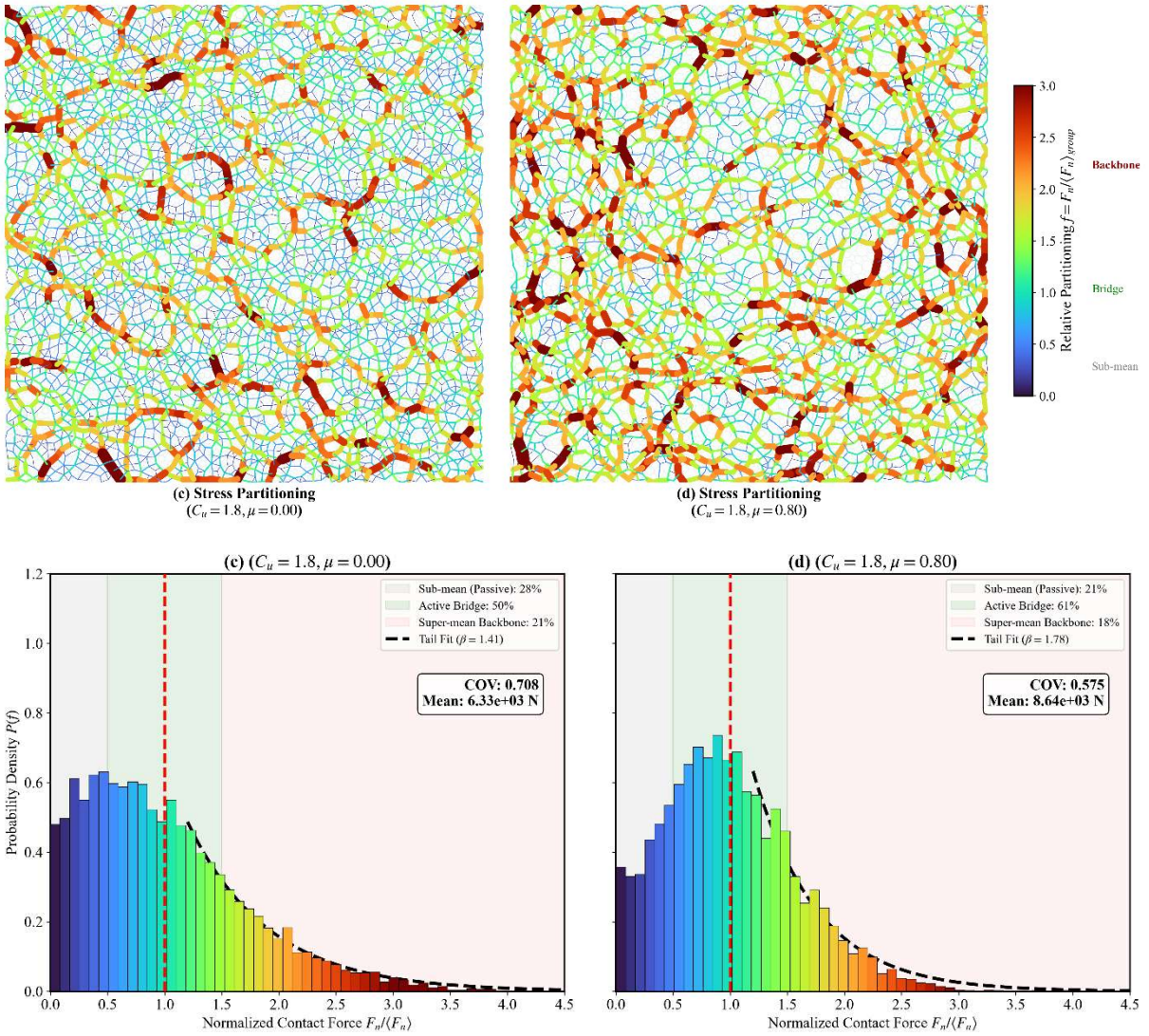

Figure 9. Force chain networks and force probability distributions for medium PSD ($C_u = 1.8$) assembly with interparticle friction coefficients of 0.00 and 0.80.

An analysis of the force distribution maps reveals that, particularly in the presence of friction ($\mu = 0.80$), certain grains (or clusters of grains) are not undergoing forces. These grains are generally smaller grains that are surrounded by loops formed by strong branches of the force network, which shields them from the overall force transmission network in the assembly. This observation is supported by the findings of Desu & Annabattula(2019), who noted that smaller particles in polydisperse assemblies tend to escape primary force chains by occupying interstitial voids.

In terms of particle size polydispersity (C_u), the results show that a wide particle size distribution ($C_u = 3.09$) consistently leads to a higher number of contacts, a lower average contact force, a wider distribution of contact forces, and, consequently, higher covariance values under identical friction conditions.

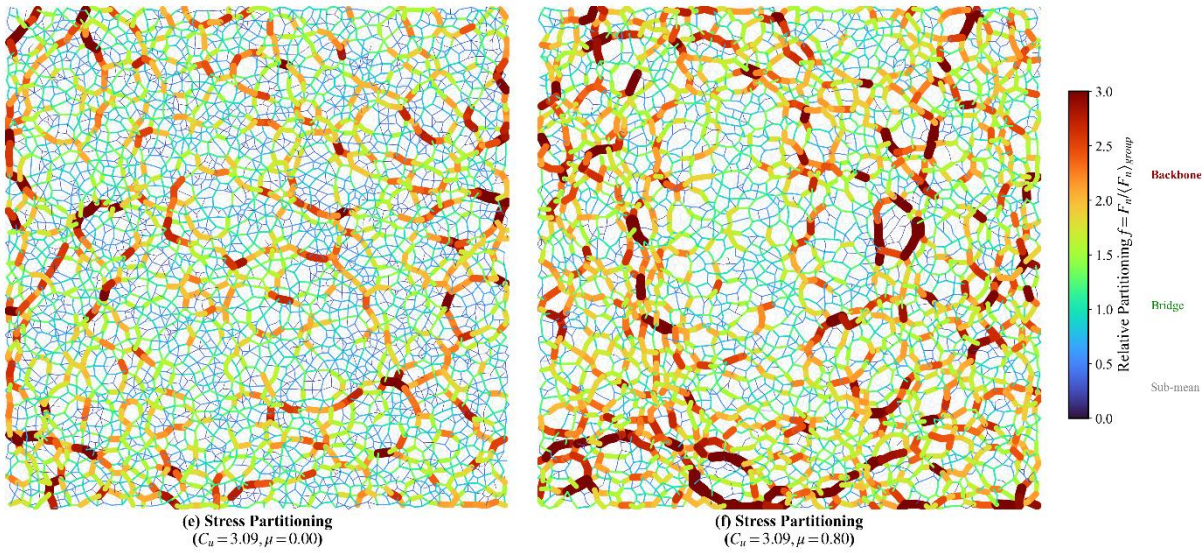

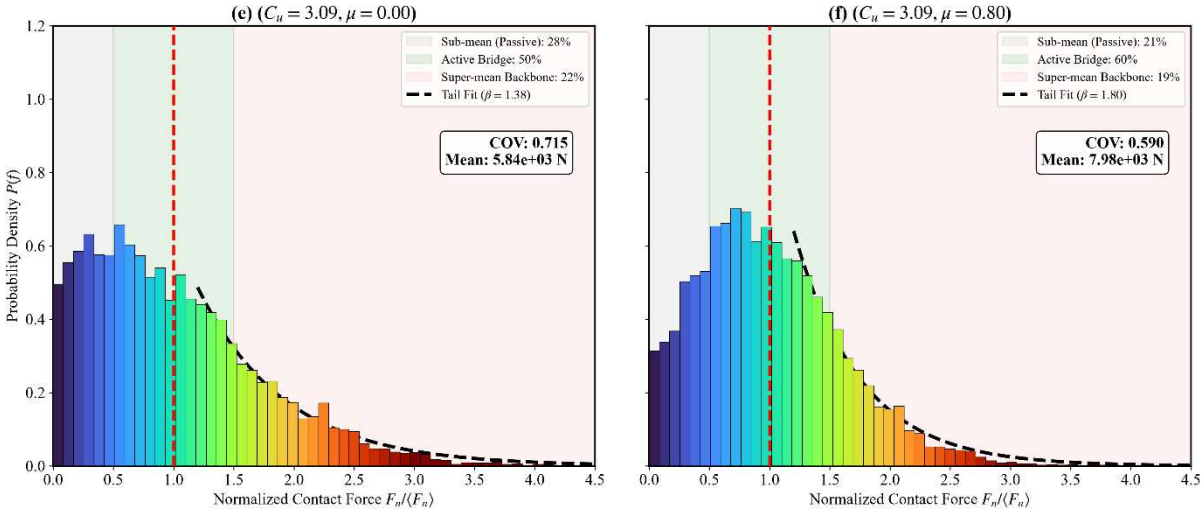

Figure 10. Force chain networks and force probability distributions for wide PSD ($C_u = 3.09$) assembly with interparticle friction coefficients of 0.00 and 0.80.

4.4 Influence of Polydispersity on Local Packing and Geometric Disorder

The objective of this section is to analyze the microstructural arrangement of the particles for the particle size distributions investigated, using Voronoi tessellation as defined in Section 3.4. The Voronoi diagrams showing the distribution of local void ratios for assemblies corresponding to the three granular distributions (narrow, medium, and wide PSDs: $C_u = 1.33, 1.80,$ and 3.09) with friction $\mu = 0.80$ under an isotropic compressive stress of 1 MPa are shown in Fig. 11. The probability densities of the local void ratios are also shown in the same figure.

Quantitatively, the results show that the $C_u = 3.09$ assembly achieves a lower global void ratio ($e = 0.223$) than the $C_u = 1.80$ ($e = 0.239$) and $C_u = 1.33$ assemblies ($e = 0.246$). This confirms that a greater diversity of particle sizes promotes more efficient filling of intergranular spaces, as smaller grains occupy the spaces between the larger particles. This is the classic "pore-filling" mechanism (Schenker et al., 2009) .

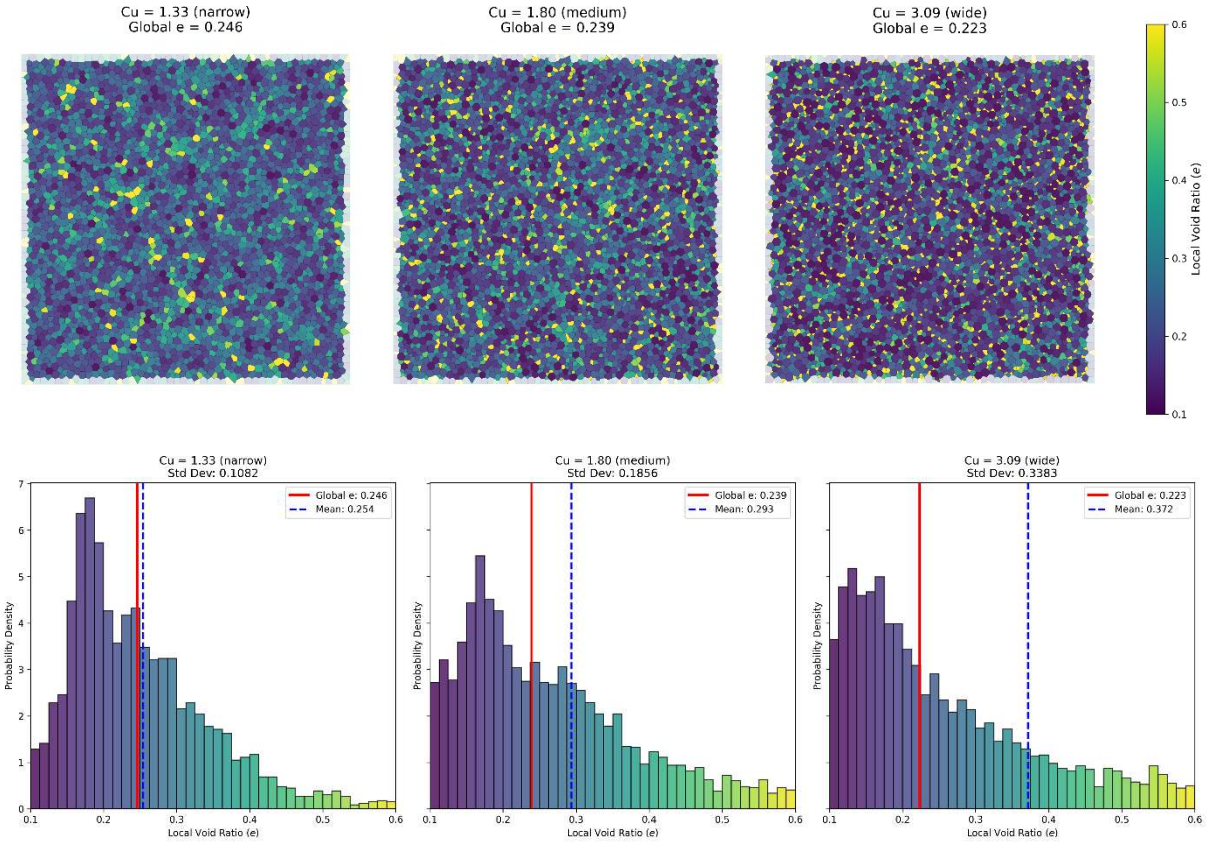

Figure 11. Voronoi Maps and statistical probability density distributions of local void ratio heterogeneity across particle size distributions ($C_u = 1.33$,1.80, and 3.09).

The data presented in the probability density plots of local void ratios show that the global void ratio is lower than the mean of local void ratios across all particle size distributions. According to the discussion in Section 3.4 regarding these quantities, this result indicates that the local void ratios associated with fine particles are higher than those associated with coarse particles. Indeed, fine particles could occupy "pockets of voids" shielded by the arcs created by the coarse particles, thus becoming associated with higher void ratios. Furthermore, it is observed that the difference between the global void ratio and the mean of the local void ratios increases progressively with broader particle size distributions (0.223 vs. 0.372 for $C_u = 3.09$, 0.239 vs. 0.293 for $C_u = 1.80$, and 0.246 vs. 0.254 for $C_u = 1.33$). This results from the relatively higher probability densities of large void ratios in the case of wider PSDs. Indeed, for broader particle distributions, the number of fine grains associated with high local void ratios is significantly greater than that corresponding to the narrow PSD.

4.5 Investigation of the relationship of microscopic topology and force transmission

This section aims to elucidate the relationship between the local packing geometry (mioscic topology) and the load transmission chains. First, the normalized average contact force per grain *is defined* as $\langle F_{n,i} \rangle / \langle F_n \rangle$, where $\langle F_n \rangle$ is the mean contact force over

the entire assembly, $\langle F_{n,i} \rangle$ being the average contact force acting on the particle i, computed as $\langle F_{n,i} \rangle = \frac{\sum F_{n,ij}}{N_{c,i}}$, with $F_{n,ij}$ as the contact force exerted by particle j on particle i and $N_{c,i}$ as the number of contacts for particle i. The ratio $\langle F_{n,i} \rangle / \langle F_n \rangle$ serves as a scalar indicator of a particle's mechanical role: if $\langle F_{n,i} \rangle / \langle F_n \rangle > 1$, the particle bears above-average loads and belongs to the "strong network" or structural skeleton; conversely, if $\langle F_{n,i} \rangle / \langle F_n \rangle < 1$, the particle belongs to the "weak network" and remains largely isolated from the principal stress transmission pathways.

Figure 12 presents the statistical distributions of the particles as a function of their mean contact force and local void ratio using a hexbin representation. The results are shown across the three particle size distributions narrow ($C_u = 1.33$), medium ($C_u = 1.80$), and wide ($C_u = 3.09$) considering a friction coefficient of $\mu = 0.80$ under an isotropic stress of 1 MPa. The color intensity represents the number of particles within each hexbin (bin width of 0.025). A curve of the mean force per void ratio interval is superimposed on the hexbin plots. The void ratio axis is subdivided into intervals 0.033 wide; the mean force is calculated as the average of the contact forces for all particles belonging to this interval.

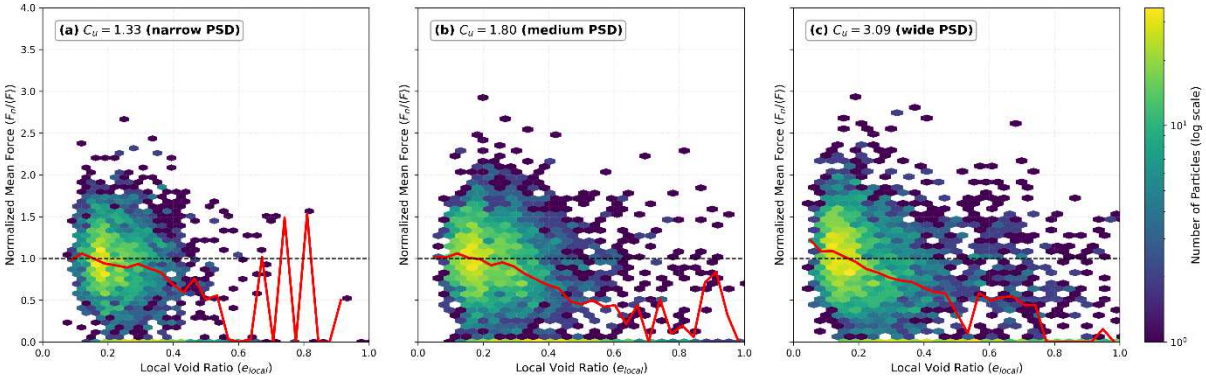

Figure 12. Hexbin representation of the statistical distribution of particles in the mean contact force–local void ratio space across particle size distributions: (a) $C_u = 1.33$ (narrow PSD), (b) $C_u = 1.80$ (medium PSD), and (c) $C_u = 3.09$ (wide PSD). The red curve indicates the mean contact force for each void-ratio interval.

Examination of these representations leads to the following main observations:

(1) For the narrow PSD ($C_u = 1.33$), the minimum local void ratio is approximately 0.10, whereas for the medium ($C_u = 1.80$) and wide ($C_u = 3.09$) PSDs, it decreases down to about 0.05. In the broader cases, these very low local void ratios are most likely associated with large particles surrounded by numerous smaller particles of varying sizes, which are more abundant in these distributions. This configuration promotes a denser local packing. On the other side of the plots, broader PSDs ($C_u = 1.80$ and $C_u = 3.09$) exhibit a progressively larger population of particles with high local void ratios, which extend to substantially higher values than those observed for the narrow PSD. These high

local void ratios are likely associated with small particles located within local void pockets formed and shielded by the surrounding larger particles.

(2) For a given local void ratio, the normalized average contact force per particle exhibits a wide range of values, from almost zero to more than twice the average force. This large dispersion suggests that the contact force experienced by a particle is poorly correlated with the local packing density. Hence, force transmission appears to be only weakly correlated with the local density state.

(3) The mean contact force computed within each void-ratio interval slightly exceeds the global average for low void ratios before decreasing progressively with increasing void ratio, ultimately reaching zero. This result indicates that, on average, the strongest contact forces are associated with particles with the lowest void ratios (i.e., particles located in the densest regions). This means that the strong network of contact forces passes primarily through particles located in dense regions (i.e., well-confined particles), but it also contains branches passing through "bridge particles," which span local voids and are associated with high void ratios, as shown in the hexbin plots.

(4) The decrease in the average contact force with increasing void ratio is much more abrupt for the narrow PSD ($C_u = 1.33$) than for the medium ($C_u = 1.80$) and wide ($C_u = 3.09$) PSDs. In the broader distributions, a significant number of particles with high void ratios still carry contact forces. Although some of these particles sustain relatively large loads, low-force particles become increasingly predominant as the void ratio increases, resulting in a gradual decrease in the average contact force. In contrast, for the narrow PSD, load-bearing particles with high void ratios become increasingly scarce, leading to a sharp reduction in the mean force. It should be noted that the fluctuations observed in the mean force curves at high void ratios arise from the limited number of particles contributing to the statistical average. These particles can be regarded as isolated statistical events and therefore have a negligible influence on the overall trend.

5. Conclusion

This study presents a micromechanical investigation of the compressibility of granular materials based on 2D DEM simulations of isotropic compression tests. Particular attention is given to the influence of interparticle friction and PSD on both the macromechanical and micromechanical responses. To this end, isotropic compression tests were performed on granular assemblies with three particle size distributions (narrow PSD, medium PSD, and wide PSD) and a range of interparticle friction coefficients. The simulations show that increasing the confining stress decreases the global void ratio, increases the mechanical coordination number, and reduces the fraction of rattler particles. In addition, for a given confining stress, assemblies with a narrow PSD exhibit higher void ratios than those with a wide PSD. Likewise, increasing the interparticle friction coefficient results in a higher void ratio. The semi-logarithmic relationship between global void ratio and confining stress clearly distinguishes the two

characteristic stages of compressibility: the recompression stage and the virgin compression stage, the latter being governed by plastic deformation induced by interparticle sliding and particle rearrangements. The calculated virgin compression indices further indicate that initially looser packings undergo greater volumetric compression during virgin compression, irrespective of whether the loose initial structure results from a higher interparticle friction coefficient or a narrower particle size distribution.

The analysis of contact-network topology demonstrates that the global void ratio is closely related to the population of elementary loops. Frictionless assemblies are dominated by triangular loops ($L = 3$), which represent the densest local packing configuration. Increasing interparticle friction promotes the persistence of larger loops ($L \geq 4$), forming stable structural arches that preserve local voids under confining pressure.

Force-chain analysis at a fixed confining stress shows that increasing interparticle friction reduces the number of contacts, thereby decreasing the connectivity of the force-chain network while increasing the average contact force. Consequently, the contact-force distribution becomes more concentrated around its mean. On the other hand, a wider PSD promotes a denser contact network, lower average contact forces, and a broader distribution of contact forces.

Although a wide PSD produces a denser global packing through a pore-filling mechanism, it also generates pronounced local packing heterogeneity. Voronoi tessellation analysis reveals the coexistence of densely packed regions and large local void pockets. Moreover, the relationship between the global and local void ratios revealed that fine particles generally exhibit higher local void ratios than coarse particles. This behaviour is attributed to the tendency of fine particles to occupy local void pockets enclosed by the surrounding coarse-particle skeleton.

Finally, The statistical distribution of particles in the mean contact force–local void ratio space was analyzed using a hexbin representation. The results show that, on average, the strongest contact forces are carried by particles with the lowest local void ratios, indicating that the force-chain network propagates predominantly through well-confined particles in the densest regions of the packing. However, the hexbin plot also reveals that some force chains extend through *bridge particles*, which span local void pockets and are characterized by relatively high local void ratios.

Collectively, these findings show that interparticle friction and particle size distribution, despite acting through distinct physical mechanisms, converge on a common topological origin for compressibility the redistribution of elementary loop sizes providing a mechanistic explanation not previously established by studying these descriptors in isolation.

Statements and Declarations Competing Interests

The authors have no competing interests to declare that are relevant to the content of this article.

Funding

No funding was received for conducting this study.

Author Contributions

Rezig Ahlem: Conceptualization, Methodology, Formal analysis, Investigation, Writing – Original Draft, Writing – Review & Editing. Mansouri Mouloud: Methodology, Formal analysis, Writing – Review & Editing. José Gregorio Gutiérrez Chacón: Supervision, Writing – Review & Editing.

Data Availability

The data generated during this study are available from the corresponding author upon reasonable request.

References

Agnolin, I., & Roux, J.-N. (2007). Internal states of model isotropic granular packings. II. Compression and pressure cycles. *Physical Review E*, *76*(6), 061303. https://doi.org/10.1103/PhysRevE.76.061303

Allen, M. P., & Tildesley, D. J. (2017). *Computer Simulation of Liquids* (Second edition). Oxford University Press.

Alshibli, K. A., & El-Saidany, H. A. (2001). Quantifying Void Ratio in Granular Materials Using Voronoi Tessellation. *Journal of Computing in Civil Engineering*, *15*(3), 232–238. https://doi.org/10.1061/(ASCE)0887-3801(2001)15:3(232)

Arévalo, R., Zuriguel, I., & Maza, D. (2010). Topology of the force network in the jamming transition of an isotropically compressed granular packing. *Physical Review E*, *81*(4), 041302. https://doi.org/10.1103/PhysRevE.81.041302

Arévalo, R., Zuriguel, I., Trevijano, S. A., & Maza, D. (2010). THIRD ORDER LOOPS OF CONTACTS IN A GRANULAR FORCE NETWORK. *International Journal of Bifurcation and Chaos*, *20*(03), 897–903. https://doi.org/10.1142/S0218127410026186

Arroyo, M., Butlanska, J., Gens, A., Calvetti, F., & Jamiolkowski, M. (2011). Cone penetration tests in a virtual calibration chamber. *Géotechnique*, *61*(6), 525–531. https://doi.org/10.1680/geot.9.P.067

667 Azéma, E., Linero, S., Estrada, N., & Lizcano, A. (2017). Shear strength and
668 microstructure of polydisperse packings: The effect of size span and shape of
669 particle size distribution. *Physical Review E*, *96*(2), 022902.
670 https://doi.org/10.1103/PhysRevE.96.022902
671 Bagi, K. (1996). Stress and strain in granular assemblies. *Mechanics of Materials*, *22*(3),
672 165–177. https://doi.org/10.1016/0167-6636(95)00044-5
673 Che, H., Yue, Y., Liu, D., & Wang, S. (2025). A Voronoi tessellation-based CFD-DEM
674 porosity model for fluidized bed modelling. *Advanced Powder Technology*, *36*(7),
675 104913. https://doi.org/10.1016/j.apt.2025.104913
676 Cundall, P. A., & Strack, O. D. L. (1979). A discrete numerical model for granular
677 assemblies. *Géotechnique*, *29*(1), 47–65.
678 https://doi.org/10.1680/geot.1979.29.1.47
679 Desu, R. K., & Annabattula, R. K. (2019). Particle size effects on the contact force
680 distribution in compacted polydisperse granular assemblies. *Granular Matter*,
681 *21*(2), 29. https://doi.org/10.1007/s10035-019-0883-9
682 Fu, R., Hu, X., Yang, B., Wang, H., & Zhou, B. (2021). An insight into the meso-scale
683 topological structure nature of granular materials subjected to quasi-static
684 shearing. *Computers and Geotechnics*, *137*, 104257.
685 https://doi.org/10.1016/j.compgeo.2021.104257
686 He, J., Han, Y., Zhang, L., & Deng, G. (2022). *Revealing Correlations Between Size*
687 *Polydispersity and Deformability of Idealized Granular Materials using DEM*. In
688 Review. https://doi.org/10.21203/rs.3.rs-1291542/v1

689 Jiang, M., Shen, Z., & Wang, J. (2015). A novel three-dimensional contact model for
690 granulates incorporating rolling and twisting resistances. *Computers and*
691 *Geotechnics*, *65*, 147–163. https://doi.org/10.1016/j.compgeo.2014.12.011
692 Khellaf, A., & Mansouri, M. (2024). Development of the stick-slip friction model for
693 discrete elements modeling. *Technology Audit and Production Reserves*,
694 *4*(1(78)), 17–25. https://doi.org/10.15587/2706-5448.2024.310428
695 Kruyt, N. P., & Rothenburg, L. (2014). On micromechanical characteristics of the critical
696 state of two-dimensional granular materials. *Acta Mechanica*, *225*(8), 2301–
697 2318. https://doi.org/10.1007/s00707-014-1128-y
698 Kuhn, M. R. (1999). Structured deformation in granular materials. *Mechanics of*
699 *Materials*, *31*(6), 407–429. https://doi.org/10.1016/S0167-6636(99)00010-1
700 Liu, J., Wu, X., Jiang, J., Ding, Z., Lü, C., & Shi, X. (2023). A network-based investigation on
701 the strong contact system of granular materials under isotropic and deviatoric
702 stress states. *Computers and Geotechnics*, *153*, 105077.
703 https://doi.org/10.1016/j.compgeo.2022.105077
704 Mansouri, M. (2014). *Hydromécanique des milieux granulaires saturés par une approche*
705 *micromécanique couplée Eléments Discrets / Lattice Boltzmann—Applications à*
706 *la géotechnique*. Université Mohamed Khider - Biskra.
707 Meng, Y., Zhu, H., Kwok, C. Y., Kuo, M., Jing, L., & Huang, X. (2018). Effect of coefficient of
708 friction on arch network in shearing process under low confinement. *Powder*
709 *Technology*, *335*, 1–10. https://doi.org/10.1016/j.powtec.2018.05.002
710 Monti, J. M., Clemmer, J. T., Srivastava, I., Silbert, L. E., Grest, G. S., & Lechman, J. B.
711 (2022). Large-scale frictionless jamming with power-law particle size

distributions. *Physical Review E*, *106*(3), 034901. https://doi.org/10.1103/PhysRevE.106.034901

Nawaz, S., & Combe, G. (2021). Sample preparation of dense granular materials Influence of void ratio *e* and coordination number Z^* on the mechanical behaviour at failure. *EPJ Web of Conferences*, *249*, 02012. https://doi.org/10.1051/epjconf/202124902012

Nguyen, T.-K., & Vo, T.-T. (2023). Effects of intergranular friction and grain size distributions on the initial void ratio of granular sample. *Journal of Science and Technology in Civil Engineering (STCE) - HUCE*, *17*(2), 110–119. https://doi.org/10.31814/stce.huce2023-17(2)-10

O'Hern, C. S., Silbert, L. E., Liu, A. J., & Nagel, S. R. (2003). Jamming at zero temperature and zero applied stress: The epitome of disorder. *Physical Review E*, *68*(1), 011306. https://doi.org/10.1103/PhysRevE.68.011306

Papadopoulos, L., Porter, M. A., Daniels, K. E., & Bassett, D. S. (2018). Network analysis of particles and grains. *Journal of Complex Networks*, *6*(4), 485–565. https://doi.org/10.1093/comnet/cny005

Radjai, F., Wolf, D. E., Jean, M., & Moreau, J.-J. (1998). Bimodal Character of Stress Transmission in Granular Packings. *Physical Review Letters*, *80*(1), 61–64. https://doi.org/10.1103/PhysRevLett.80.61

Saidani, D., Mansouri, M., & Khellaf, A. (2022). Analysis of the preloading effect on shear strength for dense sandy soils A discrete element modeling. *Innovative Infrastructure Solutions*, *7*(1), 81. https://doi.org/10.1007/s41062-021-00680-0

734 Salot, C., Gotteland, P., & Villard, P. (2009). Influence of relative density on granular
735 materials behavior: DEM simulations of triaxial tests. *Granular Matter*, *11*(4), 221–
736 236. https://doi.org/10.1007/s10035-009-0138-2
737 Schenker, I., Filser, F. T., Aste, T., Herrmann, H. J., & Gauckler, L. J. (2009). Quantification
738 of the Heterogeneity of Particle Packings. *Physical Review E*, *80*(2), 021302.
739 https://doi.org/10.1103/PhysRevE.80.021302
740 Shen, C., Liu, S., & Wang, Y. (2017). Microscopic interpretation of one-dimensional
741 compressibility of granular materials. *Computers and Geotechnics*, *91*, 161–168.
742 https://doi.org/10.1016/j.compgeo.2017.07.010
743 Silbert, L. E., Grest, G. S., & Landry, J. W. (2002). Statistics of the contact network in
744 frictional and frictionless granular packings. *Physical Review E*, *66*(6), 061303.
745 https://doi.org/10.1103/PhysRevE.66.061303
746 Thornton, C. (2000). Numerical simulations of deviatoric shear deformation of granular
747 media. *Géotechnique*, *50*(1), 43–53. https://doi.org/10.1680/geot.2000.50.1.43
748 Tordesillas, A. (2007). Force chain buckling, unjamming transitions and shear banding in
749 dense granular assemblies. *Philosophical Magazine*, *87*(32), 4987–5016.
750 https://doi.org/10.1080/14786430701594848
751 Voivret, C., Radjaï, F., Delenne, J.-Y., & El Youssoufi, M. S. (2007). Space-filling properties
752 of polydisperse granular media. *Physical Review E*, *76*(2), 021301.
753 https://doi.org/10.1103/PhysRevE.76.021301
754 Zhang, N., Hedayat, A., Han, S., Yang, R., Bolaños Sosa, H. G., González Cárdenas, J. J.,
755 & Salas Álvarez, G. E. (2021). Isotropic compression behavior of granular
756 assembly with non-spherical particles by X-ray micro-computed tomography and

discrete element modeling. *Journal of Rock Mechanics and Geotechnical Engineering*, *13*(5), 972–984. https://doi.org/10.1016/j.jrmge.2021.04.005

Zhang, T., Zhang, C., Yang, Q., & Fu, R. (2020). Inter-particle friction and particle sphericity effects on isotropic compression behavior in real-shaped sand assemblies. *Computers and Geotechnics*, *126*, 103741. https://doi.org/10.1016/j.compgeo.2020.103741

Zhang, Z., & Wang, Y.-H. (2015). Three-dimensional DEM simulations of monotonic jacking in sand. *Granular Matter*, *17*(3), 359–376. https://doi.org/10.1007/s10035-015-0562-4

Zhu, H., Nicot, F., & Darve, F. (2016a). Meso-structure organization in two-dimensional granular materials along biaxial loading path. *International Journal of Solids and Structures*, *96*, 25–37. https://doi.org/10.1016/j.ijsolstr.2016.06.025